Environmental Fluid Mechanics (2020) 20:145–164
https://doi.org/10.1007/s10652-019-09703-y

ORIGINAL ARTICLE

A comparative study of rigid-lid and level-set methods for LES of open-channel flows: morphodynamics

Ali Khosronejad[1] · Mahsa Ghazian Arabi[1] · Dionysios Angelidis[1] · Elaheh Bagherizadeh[1] · Kevin Flora[1] · Ali Farhadzadeh[1]

Received: 1 August 2018 / Accepted: 24 June 2019 / Published online: 2 July 2019

Abstract

Computational modeling of open-channel flows is usually carried out using the rigid-lid (RL) assumption to prescribe the water surface. Such an approach deems more appropriate for sub-critical flow regimes with Froude number $\ll 1$. When the Froude number is locally high, e.g. flows around hydraulic structures, the free-surface fluctuations affect the induced hydrodynamics. Indeed, prior investigations on the effect of the RL assumption on large-eddy simulation (LES) of open-channel flows around bridge abutments revealed that such an assumption may influence both the first and second order turbulence statistics. In this work, we investigate the effect of the RL assumption on bed-morphodynamics calculations. The fully coupled flow and bed morphodynamics virtual flow simulator (VFS-Geophysics) model is herein employed to numerically investigate the sediment transport around a laboratory-scale model of abutment. Numerical simulations using a mass-conserving level-set (LS) method and a RL assumption are performed to evaluate the influence of free-surface elevation on the computed bed-morphodynamics at a Reynolds number of 7.9×10^4. We also conducted an experimental study to observe the scour development around the abutment model. The instantaneous scour patterns and bed profiles computed with the LS and RL are compared with the measurements. The mean absolute errors of bed-profile predictions at or near quasi-equilibrium of bed evolution, for the LS and RL computed results, are about 4.1% and 4.7%, respectively. Despite the differences in flow field computations of the two methods, the computed bed morphology appeared relatively insensitive to the two numerical approaches. However, the computational cost of the coupled LES-LS-morphodynamics is at least one order of magnitude greater than that of the LES-RL-morphodynamics.

Keywords Level-set method · Rigid-lid assumption · LES · Bridge scour · Sediment transport · Open-channel flow

✉ Ali Khosronejad
ali.khosronejad@stonybrook.edu

[1] Civil Engineering Department, Stony Brook University, Stony Brook, NY, USA

1 Introduction

Scour pattern prediction around hydraulic structures is a crucial and challenging task in hydraulic and environmental engineering. For decades, hydraulic engineers and environmentalists have studied scour patterns around bridge abutments. Previous studies have greatly contributed to the status quo of our knowledge vis-à-vis scour process past bridge foundations. Among past studies are experimental and field investigations [1–20]. However, practical difficulties associated with scaling effects and high cost of field- and laboratory-scale studies resulted in a tendency towards utilization of numerical frameworks in order to predict the hydrodynamics and morphodynamics around bridge abutments in mobile-bed channels [20–32].

All the above mentioned studies rely on the rigid-lid (RL) method, which essentially assume that the fixed free-slip boundary condition is adequate for turbulent bed-morphodynamics calculations. The RL assumption in coupled flow and bed-morphodynamics numerical simulations is usually selected to perform low computational cost computations against free-surface resolving numerical methods. In fact, the RL assumption does not allow for self-adjustment of the free-surface in response to local acceleration induced by bridge foundations. This limitation influences the calculated turbulence statistics [33, 34] and potentially bed-morphodynamic calculations. Recently, Kara et al. [33] investigated numerically the effects of RL assumption on flow field around a laboratory-scale abutment at a Reynolds number of $Re = 6.1 \times 10^3$ and concluded that the RL assumption affects the second order statistics of turbulence obtained with large-eddy simulations (LES). In their work, the ratio of the abutment length to the mean-flow depth was $L/H = 2.6$. Khosronejad et al. [34] replicated the work of Kara et al. [33] by scaling up the flow and geometry of channel/abutment to reach a Reynolds number of 7.9×10^4 (corresponding to natural open channel flows) and L/H of 2.5. These studies revealed that the surface resolving methods affect both the computed first order and second order turbulence statistics by providing more accurate results. Recently, Kang and co-workers [35] utilized a novel method to demonstrate that slight water-surface deformation due to changes in Froude number (while keeping L/H constant and equal to 1.4) have negligible effects on the dimensionless flow field around a physical model of spur dike. Their findings suggested that for such smaller L/H ratios the RL assumption may have little effect on the dimensionless flow field. In their conclusion, they pointed to the need for further research to address the impact of the free-surface deformation on the sediment transport computations. And, to the best of our knowledge, no prior study has directly investigated the effects of free-surface prescribing methods on the morphodynamics calculations around bridge abutments.

This study presents a series of fully-coupled flow and bed morphodynamics simulations to investigate the effects of RL assumption and free-surface-resolving level-set (LS) method on sediment transport calculations around a laboratory model of bridge abutment. The studied test case represents a practical problem with a sub-critical flow regime, which is often encountered in natural sand-bed rivers and streams. We employ the coupled LES and bed-morphodynamics module of the virtual flow simulator (VFS-Geophysics) model [36–40]. Our bed morphodynamics calculations are supported by laboratory measurements in which we observed the bed deformations of the mobile bed as a result of flow acceleration around the abutment.

A series of statistical analysis enabled evaluation of the predictive errors of both LS and RL methods in computing the bed-elevation profiles around the abutment model. Our quantitative analysis showed that the mean absolute error of the bed-elevation profiles

predictions at or near quasi-equilibrium of bed-deformation process is equal to 4.1% and 4.7% for LS and RL methods, respectively. In other words, despite the influence of the free-surface approximation on the computed hydrodynamics [33, 34] and the corresponding computational cost, scour pattern predictions at or near quasi-equilibrium condition are of negligible difference. Such an observation is valuable when performing computational fluid dynamics calculations for engineering applications.

This paper is organized as follows. First, we briefly present the VFS-Geophysics numerical model. subsequently, we present a three-phase flow case the numerical simulation of which requires a free-surface tracking method. Then, we describe the experiment that was performed to generate benchmark sediment transport data. Subsequently, we present the computational details of the test cases. Finally, the experimental/numerical simulation results and the findings of the study will be presented and discussed.

2 The VFS-Geophysics model

2.1 Hydrodynamics

The equations governing the hydrodynamics include the three-dimensional spatially-filtered continuity and Navier–Stokes equations for instantaneous and incompressible flows. We solve these equations for (1) two immiscible fluids (air and water) using the LS module [41] and (2) water phase by assuming a frictionless, flat-rigid plane at the free-surface of flow in the LES mode of VFS-Geophysics code [42]. The LES turbulence model of VFS-Geophysics model is implemented in the context of the curvilinear immersed boundary (CURVIB) method [43] so that it can be applied to arbitrarily complex geometric configurations [40, 44]. The sub-grid model of constant coefficient Smagorinsky [45] method is used to account for the unresolved turbulent motions. The Navier–Stokes equations are discretized in space on a hybrid staggered/non-staggered grid arrangement [46] using a second-order accurate central differencing scheme for the convective terms along with second-order accurate, three-point central differencing for the divergence, pressure gradient and viscous-like terms. The temporal derivatives are discretized using second-order backward differencing scheme [36]. Marching in time is carried out using an efficient, second-order accurate fractional step methodology coupled with a Jacobian-free, Newton–Krylov solver for the momentum equations and a GMRES solver coupled with an algebraic multigrid pre-conditioner for solving the Poisson equation [43].

The LS equation for the water/air interface motion is discretized in space by the third-order weighted essentially non-oscillatory (WENO) scheme [47], and the discrete equation is advanced in time using the second-order Runge–Kutta method. Furthermore, the gradient term in the mass conserving reinitialization equation of the LS approach is also discretized by the second-order essentially non-oscillatory (ENO) scheme [48]. The accuracy of the free-surface algorithms for open-channel flow with complex hydraulic structures has already been verified and validated elsewhere [34, 49, 50].

2.2 Morphodynamics

Morphodynamics is modeled by considering both the bed- and suspended-loads in our continuum sediment transport module. In this model, the linkage between the LES-computed turbulence and concentration of sediment within the bed-load layer is make possible via

the mean-flow-based equation of van Rijn [51]. The temporal variation of the bed elevation is governed by the following non-equilibrium sediment continuity equation, the so-called Exner–Polya equation [37]:

$$(1-\gamma)\frac{\partial z_b}{\partial t} = \underbrace{-\nabla \cdot \mathbf{q}_{BL}}_{Bed-load} + \underbrace{D_b - E_b}_{Suspended-load} \tag{1}$$

where γ is the sediment material porosity, z_b is the bed elevation, ∇ denotes the divergence operator, $\mathbf{q}_{BL}$ is the bed-load flux vector, D_b is the net deposition onto the bed, and E_b is the net entrainment from the bed cell. The motion of sediment in suspended load is governed by the convection–diffusion equation [52]. Details of our methodology to computed the bed- and suspended-load contributions is described elsewhere [44, 53]. Herein, for clarity, we only present the method we use to couple the flow solver and morphodynamics modules at each time step of the flow solver. We use a loose-coupling bed-flow interaction approach in which flow field at time step n is employed to (1) compute the suspended sediment concentration via convection–diffusion equation and (2) interpolate the velocity components at the edge of the bed-load layer and the bed shear stress. Then, first order explicit Euler scheme is used to advance bed elevation (Eq. 1) in time, at $n+1$, as follows:

$$z_b^{n+1} = z_b^n + rhs^n(\mathbf{u}^n)\Delta t \tag{2}$$

where rhs^n is the right-hand-side of Eq. (1) calculated using velocity field ($\mathbf{u}^n$) at time step n and Δt is the time-step of the flow and morphodynamics computations. Subsequently, we use the bed deformation velocity, $w_b^{n+1} = \left(z_b^{n+1} - z_b^n\right)/\Delta t$, and the newly obtained bed geometry, z_b^{n+1}, to solve the flow governing equations at time step $n+1$, as follows:

$$\mathbf{u}^{n+1} = \mathbf{u}^n + RHS^n\left((\mathbf{u},\mathbf{p})^n, z_b^{n+1}, w_b^{n+1}\right)\Delta t \tag{3}$$

where RHS^n is the right-hand-side of the Navier–Stokes equation computed using the velocity ($\mathbf{u}$) and pressure ($\mathbf{p}$) fields at time n, bed elevation (z_b^{n+1}) and bed-deformation velocity (w_b^{n+1}) at time $n+1$.

The effect of surface slope on the initiation of the sediment particles mobility is considered by correcting the critical bed shear stress [37]. In additions, to avoid the surface slope of the mobile bed exceeding the sediment material angle of repose, we employ a mass-conservative sand-slide algorithm details of which can be found in [37]. In this sand-slide model, the bed cells with slopes greater than the angle of repose are found and, subsequently, the bed slope correction procedure of sand-slide model is applied iteratively to those cells until the bed slope in all cell centroids is less than that of angle of repose. In this work, the sand-slide algorithm converges within 1–3 iterations and each iteration takes less than 0.05 s of computing clock-time to complete. A detailed description of the morphodynamics module and its components is already reported elsewhere [40].

3 Level-set method for highly-transient flows

Despite its widespread use, rigid lid assumption can only be applied to cases whereas the changes in free surface is limited. When water surface is highly transient and subject to drastic modulations, water surface tracking methods, such as level-set, are inevitably required. In this section, we provide one such case which includes transient dam break flow over mobile sand-bed channel. The selected test case was experimentally studied

by Zech et al. [54], who used a combination of equipments and cameras to measure the evolution of water surface and bed morphology during dam break problem. The experimental test was conducted in a 6.0 m long, 0.25 m wide, and 0.7 m deep channel with a mobile bed, which is consist of sand with a median grain size of 1.82 mm, density of 2680 kg/m^3, and porosity of 0.53. Upstream of the channel was filled with 0.35 m deep water and separated from dry bed downstream with a gate. Removing the gate, they created a transient wave propagating downstream causing bed erosion. They measured the water profiles and area of bed movement throughout the flume at two instants in time: $t = 0.75$ s and 1.25 s.

We employed our model to simulate the water surface flow and sediment transport of the test case using the LES and level-set methods to resolve the turbulence and water surface evolution, respectively, in a fully coupled manner with the morphodynamics module. The computational domain contains the entire flume and mobile bed. Solid surfaces are consider to be hydraulically smooth and modeled using the wall model. A grid system with 1101, 81, and 49 nodes in streamwise, vertical, and spanwise directions is employed to discretize the computational domain obtaining a roughly uniform grid resolution of ≈ 6 mm in all directions. A time step of 10^{-4} s was sued for both the flow and morphodynamic solver.

The numerical simulation were continued for 1.25 s of actual time. In Fig. 1, we compare the measured and simulated results of both water surface and bed morphology at $t = 0.75$ and 1.25 s. As seen, the LES level-set method has done a reasonably good job of capturing the evolution of free surface. The computed bed morphologies of the channel, in terms of the area of bed material movement, are in good agreement with the measured areas of bed movement.

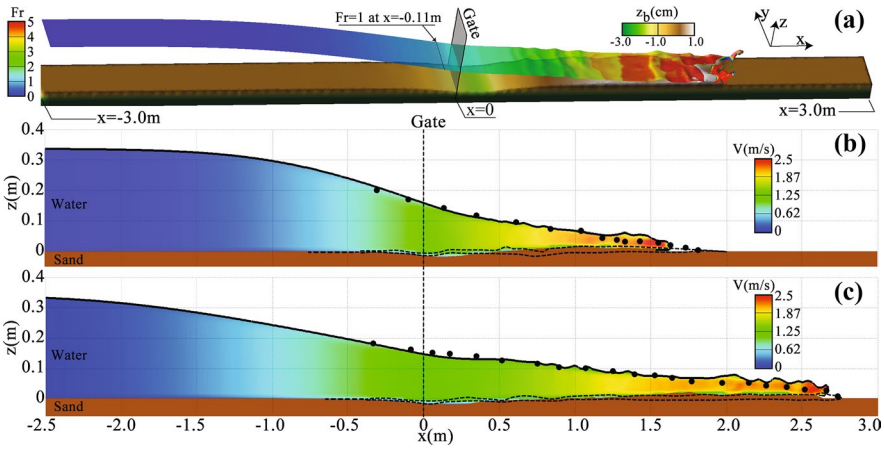

Fig. 1 Measured free surface (circles) and bed movement area (dotted dashed lines) during a dam break over mobile bed. **a** 3D view of the simulated free surface and bed elevation, in which *Fr* and z_b represent Froude number and bed surface elevation, respectively. **b**, **c** Contours of computed velocity magnitude (V) in the water phase on a longitudinal plane along the center-line of the channel. The solid lines in **b** and **c** mark the location of the computed free surface (along the center-line). The orange-colored regions at the bottom of pictures **b** and **c** depicts the computed morphology of the channel bed. **a**–**c** Correspond to $t = 0.95$ s, 0.75 s, and 1.25 s, respectively, after the removal of the gate, which is located at x = 0. Flow is from left to right

Table 1 Hydraulics and geometrical characteristics of the numerically and experimentally studied test case

Q (m^3/s)	H (m)	W (m)	L (m)	Re	Fr	d_{50} (mm)
0.15	0.2	1.5	25	$\approx 7.9 \times 10^4$	≈ 0.36	0.3

Q is the volumetric flow rate, H is the mean-flow depth, W is the channel width, L is the length of the flume, d_{50} is the median grain size of the bed material, Re is the Reynolds number, and Fr is the Froude number

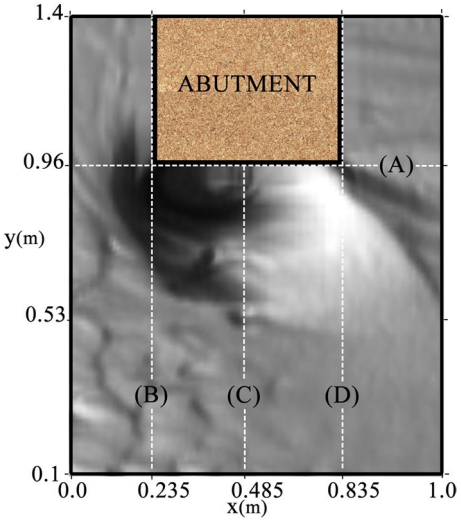

Fig. 2 The measurement window around the abutment model. We note that the flume is 1.5 m wide and 18 m long. The measured bed-elevation profiles along the four lines of (A), (B), (C), and (D) are used to compare with those obtained from numerical simulations. Flow is from left to right

4 Laboratory experiments

Experimental measurements were carried out in a 1.5 m deep mobile-bed indoor flume at the Coastal and Hydraulic Research Laboratory (CHERL) of Stony Brook University. In Table 1, we summarize the flow and geometrical parameters of the channel. The bulk velocity (U_o) of the channel flow was set equal to 0.5 m/s, resulting in Froude ($= U_o/\sqrt{gH}$) and Reynolds ($= \rho_w U_o R_h/\mu_w$, where R_h is the hydraulic radius, μ_w is the dynamics viscosity of water, and ρ_w is the density of water) numbers of ≈ 0.36 and $\approx 7.9 \times 10^4$, respectively. A 0.5 m $\times$ 0.5 m $\times$ 0.5 m cube, which represents the model of bridge abutment, was installed on the left bank of the flume. The surface of the abutment model and flume side walls are hydraulically smooth. The bottom of flume is covered with 8 cm thick, non-cohesive, uniform sediment material with a particle density of $\rho_s = 2650$ kg/m^3. Experiment started from an initially flat-mobile-bed conditions. Soon after the flow runs through channel, sediment particles are mobile and scour process commenced near the leading edge of the abutment. The data acquisition system for monitoring the evolution of bed topography includes a fully-automatic sub-mm laser scanner mounted on top of the flume. To reduce the time required for scanning the instantaneous bed topography (i.e. ≤ 1 min) while the experiment is running, the topography measurements were (1) limited to a 1.0 m (streamwise) by 1.3 m (spanwise) window around the abutment model, where the bed topography evolved most rapidly (Fig. 2), and (2) carried at time instants of $t = 3$, 8, and 18 min from beginning of the test

On the basis of our observations during the scour process, the scour pattern around the abutment model reached a quasi-equilibrium after 18 min. The resolution of the measured topography was sub-mm in vertical and ≈ 1 mm in horizontal. The measured instantaneous bed bathymetry and the bed-profiles along the four lines (a)–(d) of Fig. 2 will be presented in the next sections, where we compare the measured data with those computed by the VFS-Geophysics model.

5 Computational details

We discretized the governing equation in a computational domain that is 10 m, 1.5 m, and 0.2 m in streamwise (x), spanwise (y), and vertical (z) directions, respectively. An abutment model was installed 5 m downstream of the inlet cross-section. A mean-flow depth of 0.2 m was used in the RL-LES. An additional vertical length of 0.2 m is also considered for the air-phase domain in the LS-LES. In both RL and LS-LES, we consider an additional vertical dimension of 0.08 m on the bottom of the flume to represent the sediment layer.

In the context of the CURVIB method, single-phase flow (RL) or two-phase flow (LS) turbulent flow calculations are performed on the background mesh, while sediment transport calculations are carried out on an unstructured triangular immersed boundary (IB) surface mesh [44]. A uniformly-spaced background mesh of 5.0 mm, 7.5 mm, and 8.5 mm in streamwise, spanwise, and vertical directions, respectively, is used (see Table 2). The background mesh, therefore, consists of 13.5 and 22.9 million grid cells for the RL and LS large-eddy simulations, respectively. Since the LS-LES contains an air phase that is

Table 2 The computational grid systems and the time step employed for the flow and morphodynamics solvers using the rigid-lid (RL) and the level-set (LS) methods

	RL	LS
$N_x \times N_y \times N_z$	$1177 \times 201 \times 57$	$1177 \times 201 \times 97$
Δx (m)	8.5×10^{-3}	8.5×10^{-3}
Δy (m)	7.5×10^{-3}	7.5×10^{-3}
Δz (m)	5.0×10^{-3}	5.0×10^{-3}
Δz^+	~ 110	~ 110
Δt(s)	10^{-2}	10^{-3}
N_{G1}	19, 128	19, 128
N_{G2}	25, 769	25, 769
N_{G3}	30, 532	30, 532
ΔS_{G1}(m)	2.5×10^{-2}	2.5×10^{-2}
ΔS_{G2}(m)	2.0×10^{-2}	2.0×10^{-2}
ΔS_{G3}(m)	1.8×10^{-2}	1.8×10^{-2}

N_i and Δi ($\forall i = 1, 2, 3$) indicate the number of grid nodes and the grid spacing of the background grid for flow solver in the i direction, respectively. x, y, and z represent streamwise, spanwise, and vertical directions, respectively. $\Delta z^+ = u_* \Delta z / \nu$ is the minimum grid spacing in the vertical direction scaled in inner wall units. Shear velocity, u_*, is calculated from wall model calculations. Δt is the temporal step. N_{Gj} is the numbers of computational nodes used for the unstructured triangular mesh system of Gj ($\forall j = 1, 2, 3$) to discretize the interface of water and sediment. ΔS_{Gj} is the mean edge size of the unstructured triangular grid Gj

as high as the mean-water depth, the computational domain in our LS-LES is double that of the RL simulation. The selected time steps used for the LS and RL computations are $\Delta t = 10^{-3}$ s and 10^{-2} s, respectively, considering stability requirements when incorporating surface-resolving methods. In all our calculations the Courant–Friedrichs–Lewy (CFL) number was ≤ 1. The background mesh was selected after sensitivity analysis of the hydrodynamics, previously reported in [34]. Herein we only present grid sensitivity analysis for the sediment transport computations.

Three unstructured surface meshes with 18,128 (grid system G1); 25,769 (grid system G2) and 30,532 (grid system G3) triangular elements are employed to discretize the surface of the abutment model, flume's mobile-bed, and sidewalls (Table 2). In order to maximize the accuracy of the projection of the bed shear stresses and velocity components onto the mobile-bed surface elements and, consequently, sediment transport calculations; we selected the spatial discretization of the bed surface to be consistent with the resolution of background grid system [37].

In our RL-LES, we use a fixed water-flow rate at the inlet and a constant flow depth is assumed throughout the simulation domain. For the LS-LES, however, while the water-flow rate at the inlet is constant in time, the water surface throughout the flume is allowed to move in the vertical direction. We note that in both simulations, the flume's bed is allowed to evolve. Therefore, in the RL-LES only the bed morphology is evolving (two-phase flow), while in the LS-LES both the free-surface and the bed morphology of the flume are evolving (three-phase flow). The log-law of the wall is applied as the velocity boundary condition at the rigid surfaces of the abutment, mobile-bed of the flume, and sidewalls [40]. Numerical simulations are carried out on Zagros supercomputing cluster at the Department of Civil Engineering of Stony Brook University. Zagros has 76 compute nodes and a total of 1216 cores of 3.06 GHz Intel X5675 with 6 GB RAM/core and QDR Infiniband. The cluster has a 75 TB Lustre-based storage system with distributed meta data servers (MDS) and object storage servers (OSS), all connected via the IB network in order to handle high I/O needs of the VFS-Geophysics code. The coupled morphodynamics and LES are run for about 18.0 mm of physical time. It is important to mention that the computations for the RL-LES morphodynamics are carried out on 160 cores for about 7 days of clock-time. The LS-LES morphodynamics computations, however, are executed on 180 cores and continued for about 47 days. The disparity in clock-time required for the two simulations is expected as the time-step of the latter case is one order of magnitude smaller compared to the former case (see Table 2). The reason for the long clock-time of LS computations is twofold: (1) rapid fluctuations on the resolved free-surface require, generally, smaller time step to ensure stability of the LS simulations and (2) LS method requires solution of the Jacobi–Hamilton equation and re-initialization of the distance function, which is time consuming [50].

In order to set the initial condition for the coupled flow and bed morphodynamics simulations, we start the turbulent flow computations by allowing no bed-deformation in the channel. The flow field calculations without bed-deformation are continued for one flow-through physical time (i.e. the time required for a water particle to travel through the length of the flume). Then the flow field and water surface elevations (in LS-LES) at this time are saved and used as the initial flow field for the coupled flow-bed morphodynamics simulations.

6 Results and discussions

6.1 Hydrodynamics

The effect of the RL assumption on the hydrodynamics around the abutment of the current test case was previously studied by Khosronejad et al. [34], in which the channel-bed was rigid. They investigate the RL effect on the LES of the flow field by comparing the RL and LS computed results for the first and second order turbulence statistics. For the main part, it was shown that the acceleration of the flow at the constricted region (between the face of the abutment and the right-bank of the channel) led to an increase in the streamwise velocity of both the RL and LS computations. In the same region, however, the LS obtained flow field corresponds streamwise velocities that are about 15% more than those of the RL, owing to the water surface drop in the LS computations.

In Fig. 3, we plot the contours of the computed instantaneous Froude numbers around the abutment before activating the sediment transport module, i.e. $t = 0$. The LS computed free surface includes regions with high Froude numbers of up to 0.96. The locally high Froude numbers are limited to the areas around the leading edge of the abutment. Soon after activating the morphodynamics module, the bed morphology of the channel starts to evolve and adjust itself with the flow condition. The changes in the bed morphology of the channel are expected to alleviate the difference between the flow fields of the RL and LS methods. This could be confirm by examining the flow field of the two methods after the bed morphology of the channel reaches quasi-equilibrium. For example, Fig. 4 depicts the LES results of the instantaneous velocity magnitude, obtained from the RL and LS methods, through the channel after 18 min of sediment transport and scour development around the abutment. As seen, the two methods seem to obtain similar flow pattern with comparable velocity distributions and magnitudes.

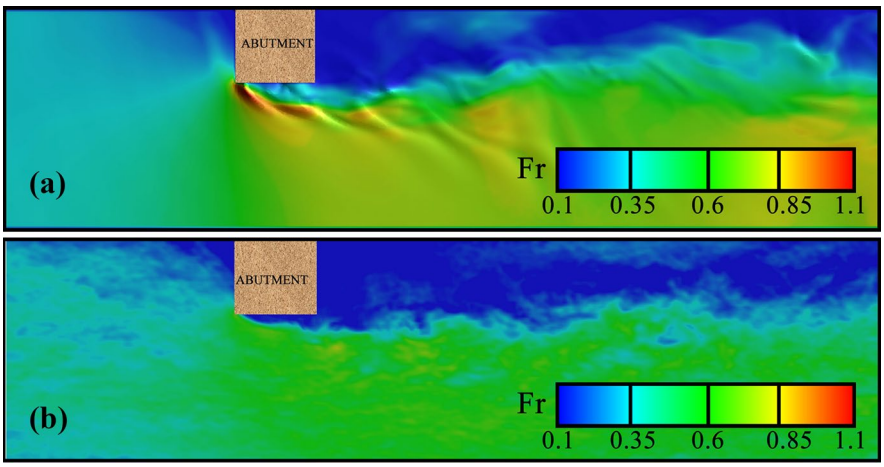

Fig. 3 Contours of instantaneous Froude number prior to activation of sediment transport module, which represents $t = 0$ of morphodynamics calculations when channel bed is flat. **a** Shows the LS computed free surface of the flow, while **b** represents the computed Froude number with the RL assumption. Flow is from left to right

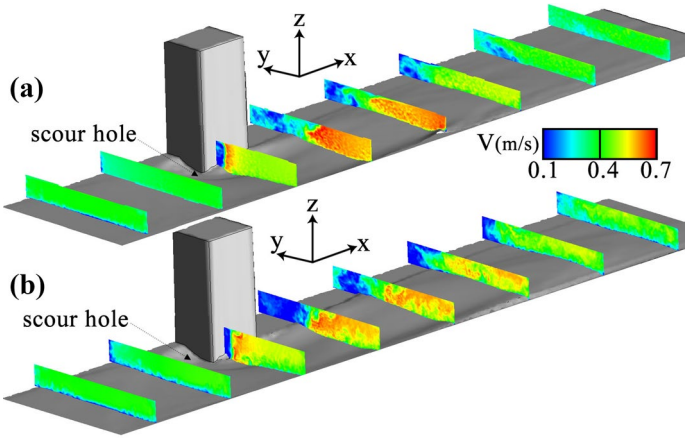

Fig. 4 Contours of LES computed instantaneous velocity magnitude (V) at seven transects along the channel after $t = 18$ min of scour process when the bed topography is at quasi-equilibrium. **a**, **b** Correspond to the LS and RL methods, respectively. Flow is from left to right

In addition, to quantify the disparity among the velocity field of the RL and LS methods at equilibrium, we depth-averaged the finite time-averaged LES results of the velocity magnitude at $t = 18$ min. The finite time-averaged results are obtained by time averaging the computed flow field over a short time window of 5 s: from $t = 1080$ to 1085 s, during which the bed topography of the channel was assumed to be frozen at $t = 18$ min. The time window of 5 s is short enough to ensure that the changes in bed geometry are minimal. The depth- and finite time-averaged velocity magnitudes of the two methods are then used to extract the velocity profiles along the three lines of (a), (b) and (c) in Fig. 2. As shown in Fig. 5, the depth- and finite time-averaged velocity magnitudes of the two methods are quite similar with a mean-absolute-error and a maximum error of about 2 and 4 percent, respectively.

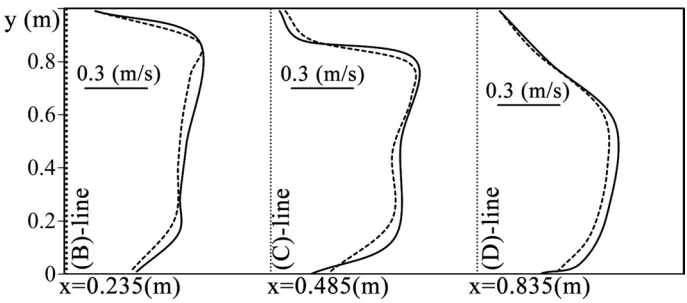

Fig. 5 Profiles of the depth- and finite time-averaged velocity magnitudes along (A), (B), and (C) lines of Fig. 2. The finite time-averaging is carried out over a time window of 5 s, starting from $t = 18$ min to 18 min and 5 s. Solid and dashed lines correspond to the RL and LS computed velocity magnitudes, respectively. y is the coordinate across the channel

6.2 Morphodynamics

We start the morphodynamics discussion by presenting the results of the grid sensitivity analysis. The structured background mesh is selected after a series of grid sensitivity analysis for the flow field computations; previously reported by Khosronejad et al. [34]. In order to examine the sensitivity of the computed morphodynamics results to the bed-surface grid resolution, we focus on the unstructured triangular grid system. The coupled flow and bed morphodynamics simulations are continued for 3 min of physical time on three unstructured triangular grid systems, denoted as G1, G2, and G3. We plot in Fig. 6 the computed instantaneous bed-elevation profiles obtained with the G1, G2, and G3 grid systems. It is evident from Fig. 6 that the morphodynamics results of grid systems G1 to G3 are not fully converged. However, the figure shows that the results of the three grid systems, from G1 to G3, follow a converging trend. Therefore, the grid system G3 (i.e. the finest grid) was

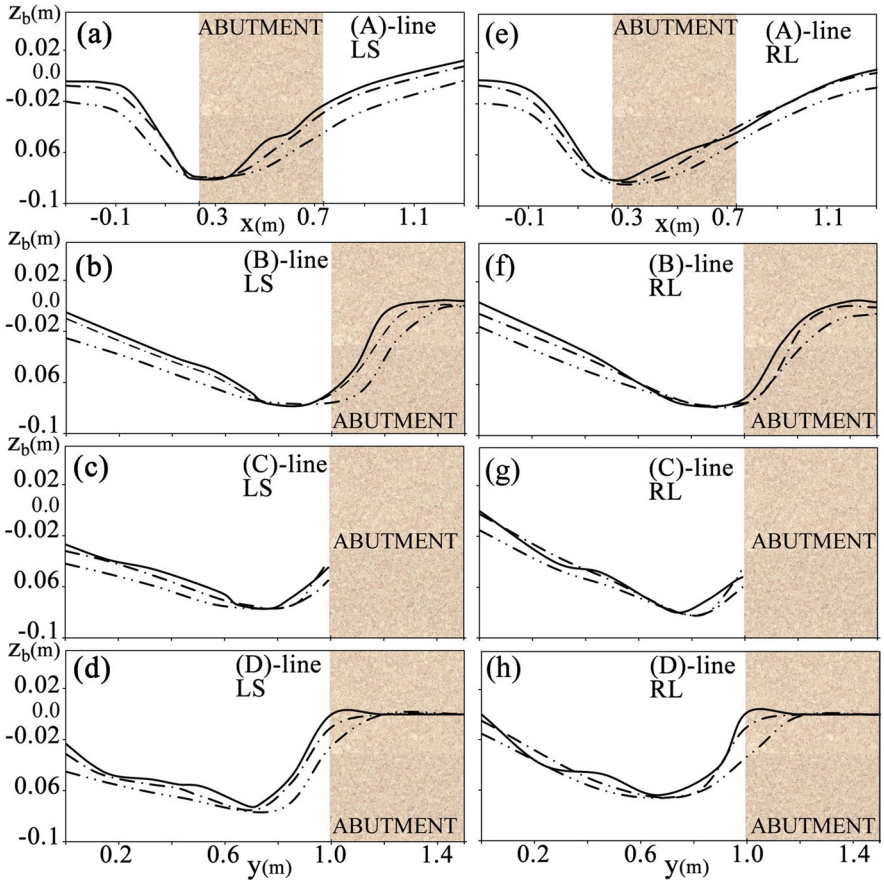

Fig. 6 Grid sensitivity analysis of the computed instantaneous bed-profiles at $t = 3$ min. **a**–**d** Show the LS (LS) computed results, while **e**–**h** correspond to the RL computations. Simulated bed-profiles are obtained along the (A)-line to (D)-line, as shown in Fig. 2. Double-dotted-dashed, dotted-dashed, and bold lines corresponds to the computation results of the bed-profiles on grid systems G1, G2, and G3, respectively. It is evident that G3 unstructured mesh can provide grid independent simulations

selected to perform the coupled flow and bed morphodynamics simulations. For the sake of brevity, in the rest of paper, we only present the simulation results of the grid system G3.

In Figs. 7 and 8, we plot the computed instantaneous bed topography using LS and RL methods. Our observations show that, in both cases, local scour starts near the leading edge of the abutment and leads to formation of point bars around and downstream of the tailing edge of the abutment. Comparing the computed scour patterns in these figures, one can clearly see that the LS simulated scour pattern is more pronounced (in both depth and width) than that of RL. We argue that this is related to the flow field results and bed shear stress distribution of the LS and RL simulations. As reported by Khosronejad et al. [34], the LS computed flow field is associated with a ~ 20% drop in water depth, immediately downstream of the leading edge of the abutment. The drop in the water depth of LS simulated hydrodynamics leads to the formation of a high-velocity region with a bed shear stress magnitude greater (by about 15%) than that of RL computed flow field [34].

A qualitative comparison among the LS-computed, RL-computed, and measured scour patterns in the vicinity of the abutment model can be found in Fig. 9. We note that Fig. 9d–f are blown up of Figs. 7 and 9g–i are blown up of Fig. 8. As shown in Fig. 9a–c, the measured bed morphology can be characterized with a major scour hole and several minor scour holes (i.e. SH1, SH2, SH3, and SH4) downstream of the leading edge. The series of scour holes coincide along a straight line which make an angle of 40° with x-coordinate (see the dashed-line in Fig. 9b). Throughout the experiment and until the quasi-equilibrium state of the scour pattern, this angle is almost the same. We argue that these scour holes clearly show footprints of large-scale, high-energy vortical structures that shed

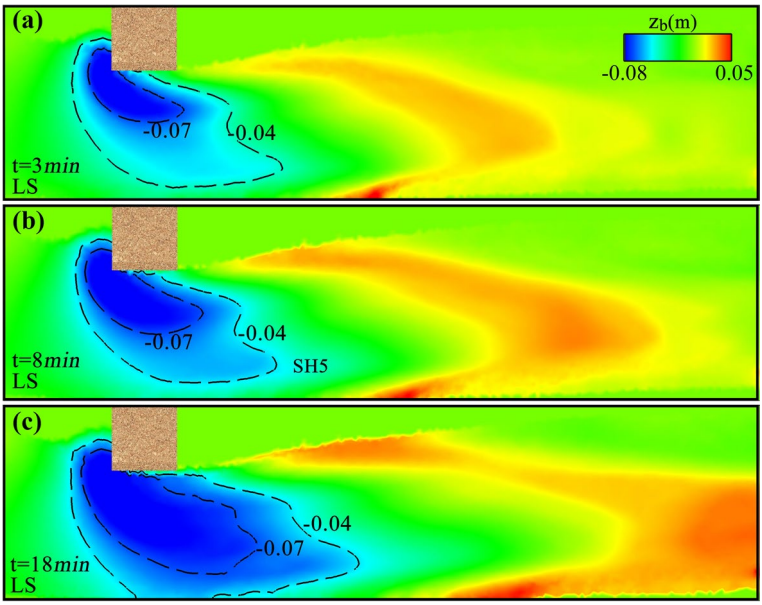

Fig. 7 Color maps of computed instantaneous bed-elevation (z_b) after **a** $t = 3$ min, **b** 8 min, and **c** 18 min using LS method. Blue region shows the scour hole region. A major scour hole zone can be seen near the leading edge of the abutment. While, a less deep scour hole region is predicted immediately downstream of the major scour hole (indicated as SH5 in **b**). A simulated sediment deposition region, which travels downstream, can be seen in the pictures. Flow is from left to right

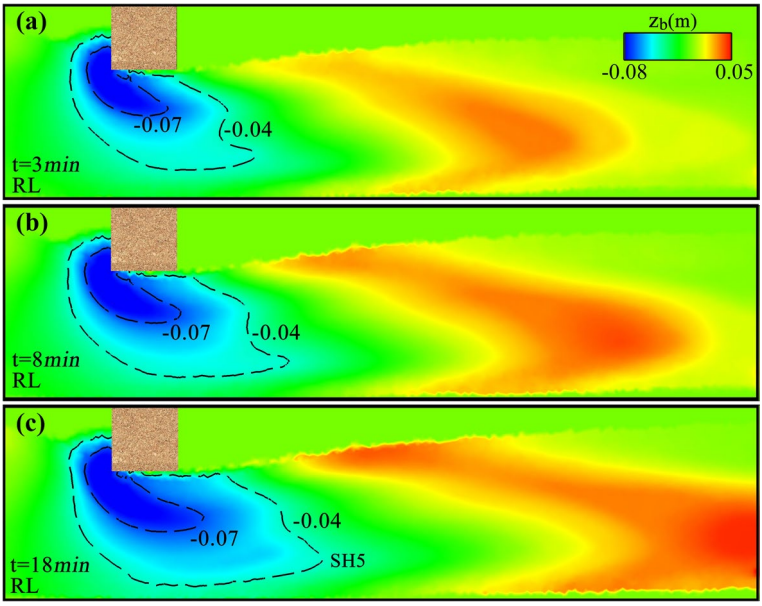

Fig. 8 Color maps of computed instantaneous bed-elevation (z_b) after **a** $t = 3$ min, **b** 8 min, and **c** 18 min using RL assumption. A major scour hole zone can be seen near the leading edge of the abutment, While a less deep scour hole region is obtained immediately downstream of the major scour hole (indicated as SH5 in **c**). Furthermore, a downstream-migrating point-bar can be seen in the pictures. Flow is from left to right

from the leading edge of the abutment. Both LS and RL computed bed morphology are in good quantitative agreement with the measured morphology (Fig. 9d–i). More specifically, the computed major scour holes in both LS and RL cases are similar to the measured one. The computed scour patterns do not include the minor scour holes like those of SH1, SH2, SH3, or SH4 in Fig. 9b. However, regions of deep scours apart from the major scour hole can be clearly seen in both LS and RL simulations. In Figs. 7 and 8, the computed minor scour regions are indicated with SH5. Therefore, as shown by the dashed-lines in Fig. 9e, h), similar straight lines can be passed through the computed minor scour regions. Furthermore, the lines in the LS and RL computed bed morphologies make angles of ~ 39° and ~ 34°, respectively. Thus, one can clearly see that the SH5 scour hole regions are diffused forms of the measured minor scour holes. Depicted in perspective 3D view, Fig. 10 also plots the scour pattern around the physical model of the abutment after $t = 18$ min. Before discussing the sources of errors that have led to the discrepancies between the measured and computed bed morphologies, we seek to compare the computed and measured results quantitatively.

In Fig. 11 we compare the measured and computed bed profiles along the four lines (a) to (d) of Fig. 2. As seen in this figure, the discrepancies between the computed LS and RL bed profiles reduce in time and reach their minimum at the quasi-equilibrium (i.e. $t = 18$ min). Additionally, the overall agreement of the computed and measured bed profiles deems to improve with the passage of time. This can be seen in the quasi-equilibrium results of Fig. 11, which show a relatively better agreement between the computed and measured bed profiles. This seems to imply that, despite our careful attention, the initial conditions of the experiential test and numerical simulations are slightly different. The fluctuations seen along the (C)- and (D)-lines of the measured bed profiles is associated

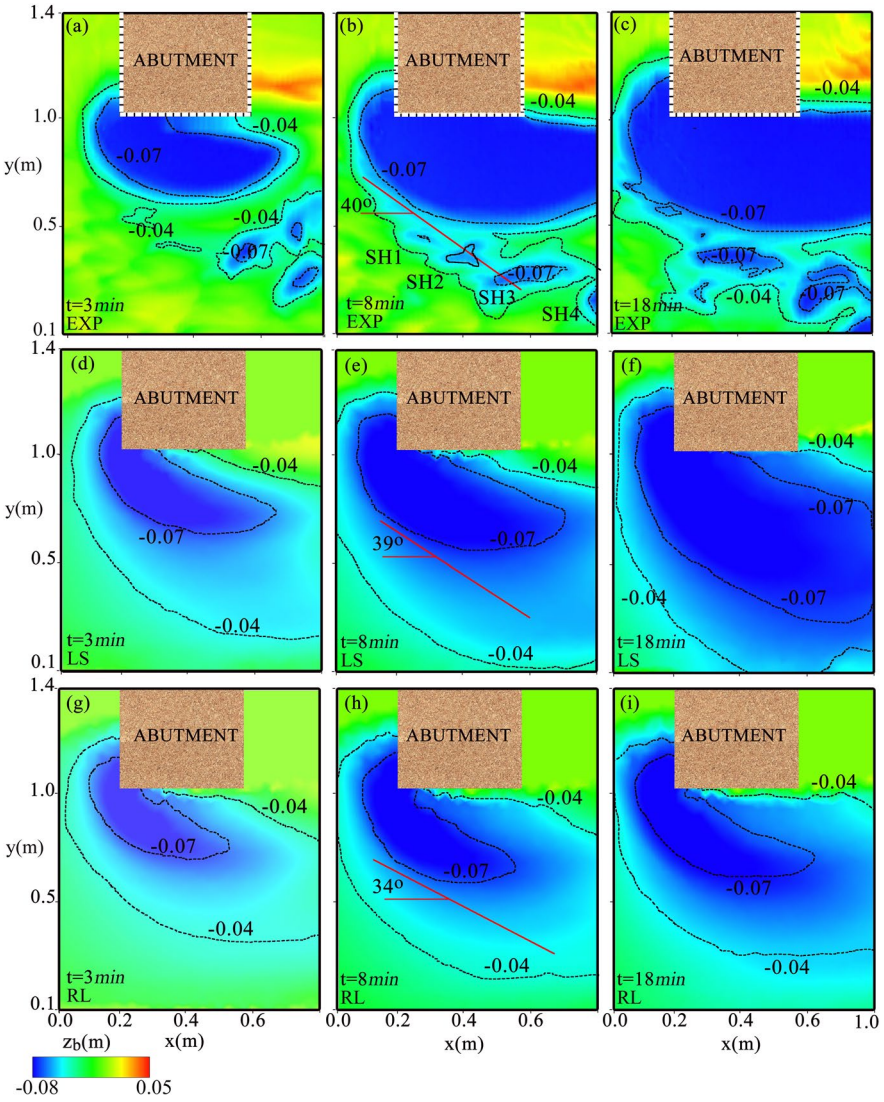

Fig. 9 Color maps of **a**–**c** measured, **d**–**f** LS computed, and **g**–**i** RL computed instantaneous bed-elevation (z_b) from top view. The color maps are limited to the horizontal window in Fig. 2. A major scour hole can be seen in all cases. Several distinctive minor scour holes–denoted as SH1, SH2, SH3, and SH4—can be only seen in the measured bed morphologies (**a**–**c**). A diffused form of minor SH*i* scour holes can be seen in the LS and RL computed bed morphologies. In **b**, **e** and **h**, we draw straight lines along the measured and computed minor scour holes. Flow is from left to right

with minor scour holes of SH1 to SH4 (Fig. 9b). In order to statistically analyze the error percentages of LS and RL computed bed profiles, we use the mean-absolute-error-percentage (*err*) and skill score (sk_{score}), which are defined as follows [55]:

$$sk_{score} = 1 - \frac{\sum(z_{model} - z_{exp})^2}{\sum(z_{exp} - \overline{z_{exp}})^2} \tag{4}$$

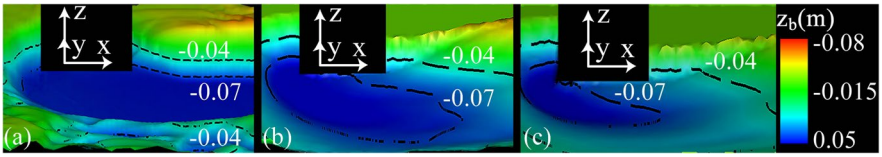

Fig. 10 Perspective 3D view of **a** measured, **b** LS computed, and **c** RL computed scour patter at the quasi-equilibrium (i.e. $t = 18$ min) around the physical model of the abutment. Flow is from left to right

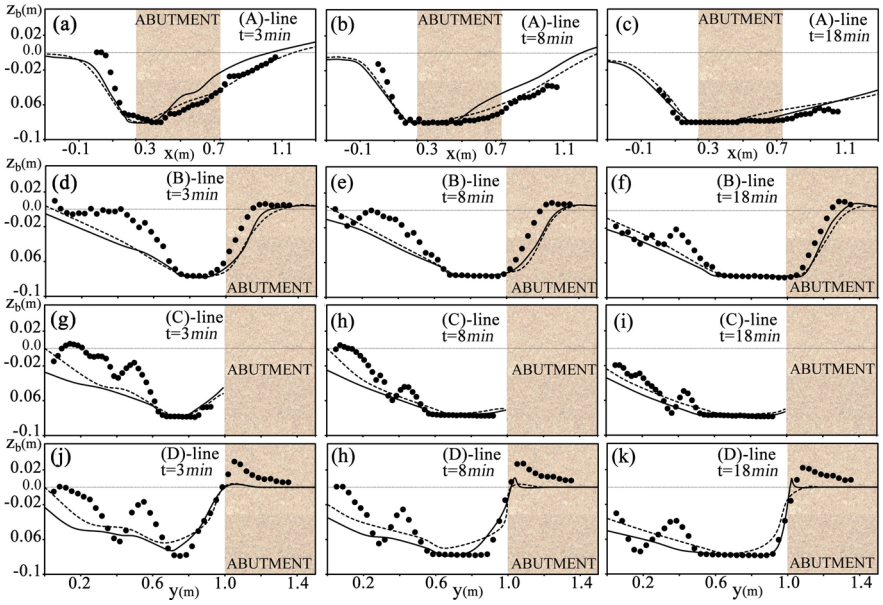

Fig. 11 Measured (dots), LS computed (solid-lines), and RL computed (dashed-lines) instantaneous bed-elevation profiles along the (A), (B), (C), and (D) lines of Fig. 2

$$err = \overline{\left| \frac{z_{model} - z_{exp}}{z_{exp}} \right|} \times 100 \tag{5}$$

where z_{exp} is the measured bed-elevation, z_{model} is the computed bed-elevation, and $\overline{z_{exp}}$ is the mean value of z_{exp}, and $\overline{|\cdot|}$ is the local mean absolute operator. Based on the above definitions, the computational err would decrease as sk_{score} increases and vice versa.

A quantitative analysis of the computed bed-elevation profiles (Fig. 11) can be done via the calculated sk_{score} and err in Tables 3 and 4, respectively. We note that the results of these tables solely refer to the comparison of the RL and LS results for the morphodynamics simulations. As shown in Table 3, the calculated sk_{score} for LS and RL computed bed profiles converges to a maximum after 18 min (quasi-equilibrium). The calculated err, on the other hand, for both the LS and RL computed profiles converges to a minimum at quasi-equilibrium (Table 4). Using the data in Tables 3 and 4, we calculated the mean values of sk_{score} and err for the LS and RL computed bed profiles at $t = 18$ min. The averaged values of sk_{score} and err [for the bed-elevation profiles along (a)–(d)-lines in Fig. 11]

Table 3 Calculated instantaneous skill score (sk_{score}) of the LS and RL predictions for the bed-elevation profiles along the four lines of (A), (B), (C), and (D) in Fig. 2

	t = 3min	t = 8min	t = 18min
(A)-line			
RL	0.57	0.80	0.89
LS	0.46	0.73	0.87
(B)-line			
RL	0.57	0.74	0.82
LS	0.44	0.73	0.83
(C)-line			
RL	0.51	0.79	0.85
LS	0.49	0.66	0.79
(D)-line			
RL	0.65	0.81	0.86
LS	0.53	0.72	0.86

Table 4 Calculated instantaneous mean-absolute-error-percentage (err) of the LS and RL predictions for the bed-elevation profiles along the four lines of (A), (B), (C), and (D) in Fig. 2

	t = 3min	t = 8min	t = 18min
(A)-line			
RL	77.1%	23.4%	13.0%
LS	83.2%	33.4%	8.5%
(B)-line			
RL	4.9%	5.1%	2.7%
LS	10.1%	6.3%	3.9%
(C)-line			
RL	4.9%	3.3%	1.5%
LS	6.1%	3.5%	2.0%
(D)-line			
RL	3.1%	2.6%	1.6%
LS	3.5%	2.9%	1.8%

are 0.84 and 4.1% for LS and 0.85 and 4.7% for RL computations, respectively. This comparison clearly shows that the quantitative disparity between the LS and RL scour pattern predictions is negligible. In Fig. 12 we also plot data-points of LS- versus RL-computed bed elevations along the lines of (a)–(d) (Fig. 11). The bed-elevation data points at quasi-equilibrium (i.e. at t = 18 min) align more closely along the 45° line that those of previous instants in time (i.e. t = 3 and 8 min). Overall, the scour pattern predictions of RL and LS methods are of approximately the same accuracy while the computational cost associated with the LS modeling is at least one order of magnitude higher than that of RL.

Finally, discrepancies in the prediction of instantaneous scour hole patterns (Fig. 9) can be attributed to error sources such as: (1) uncertainties in experimental data acquisition, (2) insufficient mesh resolution for the flow field solver, and (3) lack of a momentum equation for sediment particles transport in our continuum morphodynamics solver. The data acquisition apparatus required about a minute to complete the scan of the horizontal window around the abutment for each of the t = 3 min, 8 min, and 18 min instants (Fig. 9). Therefore, one can infer that the measured bed elevation at the beginning of the scanning for an instant t is not in perfect synchrony with the point data scanned at the end of the

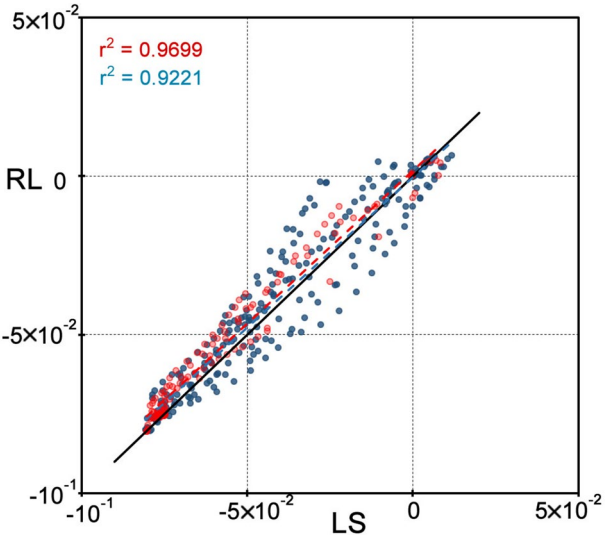

Fig. 12 Scatter-plot of RL and LS computed bed elevation (in m) at quasi-equilibrium ($t = 18$ min) (red dots) and before ($t = 3$ and 8 min) (blue dots) along the (A), (B), (C), and (D) lines of Fig. 2. Solid and dashed lines show the perfect fit and linear regressions using least-square-fit, respectively. Red and blue dashed-lines correspond to the red and blue dots, respectively. Red and blue r^2 represent the squared correlation coefficients of the red and blue dashed-lines, respectively

process. Given that the employed background grid system is not sufficiently fine to enable resolution of the viscous sub-layer of the boundary layer, we use a wall-model approach to describe the hydrodynamics effects of the dynamic bottom boundary on the flow field [37] (Table 2). Lastly, the shortcomings in our continuum bed morphodynamics module could have also contributed to the discrepancies observed in Fig. 9. A major shortcoming of the continuum morphodynamics module concerns the use of empirical and mean-flow based methods for computing the sediment bed-load flux [51, 56]. LES computed *instantaneous* flow and shear stress fields are utilized to calculate the sediment bed-load flux. But, the bed-load flux equations are based on *mean-flow* characteristics. We are currently seeking to address this shortcoming of the continuum morphodynamics by linking the bed-load flux of sediment to the instantaneous flow characteristics obtained from LES model.

7 Conclusion

Following on the two previous studies reported in [33, 34], in which the effects of rigid lid assumption on the LES computed flow field of various Reynolds numbers were examined, herein we seek to investigate the impacts of free-surface resolving techniques on the LES computed scour pattern around a laboratory-scale model of abutment at a moderate Froude number of 0.36. The test case of Khosronejad et al. [34], i.e. turbulent open-channel flow and an abutment model, with a Reynolds number of 7.9×10^4 is selected as the test-bed for the current work. We turned the rigid-bed flume of Khosronejad et al. [34] into a mobile-bed channel by placing about 8 cm thick layer of roughly uniform sand material. The mobile-bed experimental study, under live-bed condition, was carried out by allowing the scour pattern around the abutment model to reach quasi-equilibrium, which occurred after about 18 min. We employed a sub-mm scanner to measure the instantaneous bed morphology of the flume at different instants. The experimentally obtained bed morphological data were used to assess the performance of coupled LES and morphodynamcis computations with LS and RL methods.

The flow and bed morphodynamics evolution within the flume and around the abutment model were numerically simulated using the flow, sediment, and geometrical conditions identical to that of the experiment. The simulations were carried out using LES to resolve the turbulent flow field. In one case, we employed the level set method to resolve the water-surface elevation. In this case, both the water surface and the bottom boundary (mobile-bed of the flume) evolve and, thus, were solved for in a fully-coupled three-phase flow manner. In the other case, rigid lid assumption was used to prescribe the water surface. The computational costs of the level set simulations were significantly higher than that of rigid lid, almost an within order of magnitude. The scour patterns obtained by level set and rigid lid are somewhat different during the initial stages of the scour process (Fig. 11). However, once the scour pattern reached its quasi-equilibrium, the predicted results of the two methods seem to converge. Furthermore, our statistical analysis of the mean absolute error percentage and skill score for the scour pattern predictions of the two methods suggest that: (1) the simulated results of the both methods are in good agreement with the measured results and (2) the predicted bed-elevation profile of the two methods, at or near the quasi-equilibrium, are of the same order of accuracy (see Tables 3 and 4).

Hence, our findings show that the effect of water surface variations on the scour processes around hydraulic structures is insignificant and thus rigid lid assumption can be safely utilized to prescribe the free surface. Although, since this study is limited to a Froude number of 0.36, such conclusion can be made only for cases in which $Fr = 0.36$. However, as Froude number decreases, water surface variations and its effects on the flow and morphodynamics are expected to reduce [57]. Therefore, one can argue that for the open-channel flows with Froude number ≤ 0.36 rigid-lid method could be used to prescribe the water surface and such assumption will not jeopardize the accuracy of scour pattern predictions.

Finally, it should be mentioned that the current study regards the effect of rigid lid assumption on the morphodyanmics computations of LES under sub-critical flow regimes. Further research may be required to examine the same effect under super-critical flow regimes, in which greater water-surface deformations are expected.

Acknowledgements This work was supported by the NSF Award EAR-1823121. The computational resources were provided by the Center for Excellence in Wireless and Information Technology (CEWIT), College of Engineering and Applied Sciences at Stony Brook University.

References

1. Chabert J, Engeldinger P (1956) Etude des affouillements autour des piles de ponts. Lab. Natl. Hydraul., Chatou
2. Brice J, Blodgett J (1978) Countermeasures for hydraulic problems at bridges. Department of Transportation, Federal Highway Administration, Offices of Research and Development, Washington
3. Wong W (1982) Scour at bridge abutments. Technical report, Department of Civil Engineering, University of Auckland, Auckland, New Zealand
4. Kwan F (1984) Study of abutment scour. Technical report, School of Engineering, University of Auckland, Auckland, New Zealand
5. Kandasamy JK (1985) Local scour at skewed abutments. Technical report, School of Engineering, University of Auckland, Auckland, New Zealand
6. Sutherland A (1986) RRU occasional paper, National Roads Board, Wellington, New Zealand
7. Macky GH (1990) Department of Scientific and Industrial Research, Hydrology Centre, Christchurch, New Zealand
8. Melville BW (1992) Local scour at bridge abutments. J Hydraul Eng 118(4):615. https://doi.org/10.1061/(ASCE)0733-9429(1992)118:4(615)

9. Sturm TW, Janjua NS (1994) Clear-water scour around abutments in floodplains. J Hydraul Eng 120(8):956
10. Przedwojski B (1995) Bed topography and local scour in rivers with banks protected by groynes. J Hydraul Res 33(2):257. https://doi.org/10.1080/00221689509498674
11. Melville BW (1995) Bridge abutment scour in compound channels. J Hydraul Eng 121(12):863. https://doi.org/10.1061/(ASCE)0733-9429(1995)121:12(863)
12. Kandasamy JK, Melville BW (1998) Maximum local scour depth at bridge piers and abutments. J Hydraul Res 36(2):183
13. Oliveto G, Hager WH (2002) Temporal evolution of clear-water pier and abutment scour. J Hydraul Eng 128(9):811. https://doi.org/10.1061/(ASCE)0733-9429(2002)128:9(811)
14. Sumer BM, Fredsoe J (2002) The mechanics of scour in the marine environment. World Scientific Publishing, Singapore
15. Coleman SE, Lauchlan CS, Melville BW (2003) Clear-water scour development at bridge abutments. J Hydraul Res 41(5):521. https://doi.org/10.1080/00221680309499997
16. Dey S, Barbhuiya AK (2006) Velocity and turbulence in a scour hole at a vertical-wall abutment. Flow Meas Instrum 17(1):13
17. Fael CMS, Simarro-Grande G, Martin-Vide JP, Cardoso AH (2006) Local scour at vertical-wall abutments under clear-water flow conditions. Water Resour Res 42(10):W10408
18. Sturm TW (2006) Scour around bankline and setback abutments in compound channels. J Hydraul Eng 132(1):21. https://doi.org/10.1061/(ASCE)0733-9429(2006)132:1(21)
19. Ettema R, Kirkil G, Muste M (2006) Similitude of large-scale turbulence in experiments on local scour at cylinders. J Hydraul Eng 132(1):33
20. Koken M, Constantinescu G (2014) Flow and turbulence structure around abutments with sloped sidewalls. J Hydraul Eng 140(7):04014031. https://doi.org/10.1061/(ASCE)HY.1943-7900.0000876
21. Ouillon S, Dartus D (1997) Three-dimensional computation of flow around groyne. J Hydraul Eng 123(11):962. https://doi.org/10.1061/(ASCE)0733-9429(1997)123:11(962)
22. Biglari B, Sturm TW (1998) Numerical modeling of flow around bridge abutments in compound channel. J Hydraul Eng 124(2):156. https://doi.org/10.1061/(ASCE)0733-9429(1998)124:2(156)
23. Chrisohoides A, Sotiropoulos F, Sturm TW (2003) Coherent structures in flat-bed abutment flow: computational fluid dynamics simulations and experiments. J Hydraul Eng 129(3):177. https://doi.org/10.1061/(ASCE)0733-9429(2003)129:3(177)
24. Nagata N, Hosoda T, Nakato T, Muramoto Y (2005) Three-dimensional numerical model for flow and bed deformation around river hydraulic structures. J Hydraul Eng 131(12):1074. https://doi.org/10.1061/(ASCE)0733-9429(2005)131:12(1074)
25. Roulund A, Sumer BM, Fredsoe J, Michelsen J (2005) Numerical and experimental investigation of flow and scour around a circular pile. J Fluid Mech 534:351
26. Sumer BM (2007) Mathematical modelling of scour: a review. J Hydraul Res 45(6):723
27. Koken M, Constantinescu G (2008) An investigation of the flow and scour mechanisms around isolated spur dikes in a shallow open channel: 1. Conditions corresponding to the initiation of the erosion and deposition process. Water Resour Res. https://doi.org/10.1029/2007wr006489
28. Koken M, Constantinescu G (2008) An investigation of the flow and scour mechanisms around isolated spur dikes in a shallow open channel: 2. Conditions corresponding to the final stages of the erosion and deposition process. Water Resour Res. https://doi.org/10.1029/2007wr006491
29. Teruzzi A, Ballio F, Armenio V (2009) Turbulent stresses at the bottom surface near an abutment: laboratory-scale numerical experiment. J Hydraul Eng 135(2):106. https://doi.org/10.1061/(ASCE)0733-9429(2009)135:2(106)
30. Koken M, Constantinescu G (2009) An investigation of the dynamics of coherent structures in a turbulent channel flow with a vertical sidewall obstruction. Phys Fluids 21(8):085104. https://doi.org/10.1063/1.3207859
31. Koken M, Constantinescu G (2011) Flow and turbulence structure around a spur dike in a channel with a large scour hole. Water Resour Res. https://doi.org/10.1029/2011wr010710
32. Ettema R, Ng K, Chakradhar R, Fuller J, Kempema E (2015) Failure of spill-through bridge abutments during scour: flume and field observations. J Hydraul Eng 141(5). https://doi.org/10.1061/(ASCE)HY.1943-7900.0000996
33. Kara S, Kara MC, Stoesser T, Sturm TW (2015) Free-surface versus rigid-lid LES computations for bridge-abutment flow. J Hydraul Eng 141(9):04015019. https://doi.org/10.1061/(ASCE)HY.1943-7900.0001028

34. Khosronejad A, Ghazan M, Angelidis D, Bagherzade E, Flora K, Farhadzadeh A (2019) Comparative hydrodynamic study of rigid-lid and level-set methods for LES of open-channel flow. J Hydraul Eng 145(1):04018077
35. Jeon J, Lee JY, Kang S (2018) Experimental investigation of three-dimensional flow structure and turbulent flow mechanisms around a nonsubmerged spur dike with a low length-to-depth ratio. Water Resour Res 54:3530. https://doi.org/10.1029/2017WR021582
36. Kang S, Lightbody A, Hill C, Sotiropoulos F (2011) High-resolution numerical simulation of turbulence in natural waterways. Adv Water Resour 34(1):98
37. Khosronejad A, Kang S, Borazjani I, Sotiropoulos F (2011) Curvilinear immersed boundary method for simulating coupled flow and bed morphodynamic interactions due to sediment transport phenomena. Adv Water Resour 34(7):829
38. Khosronejad A, Kang S, Sotiropoulos F (2012) Experimental and computational investigation of local scour around bridge piers. Adv Water Resour 37:73
39. Khosronejad A, Hill C, Kang S, Sotiropoulos F (2013) Computational and experimental investigation of scour past laboratory models of stream restoration rock structures. Adv Water Resour 54:191
40. Khosronejad A, Sotiropoulos F (2014) Numerical simulation of sand waves in a turbulent open channel flow. J Fluid Mech 753:150
41. Osher S, Sethian JA (1988) Fronts propagating with curvature-dependent speed: algorithms based on Hamilton–Jacobi formulations. J Comput Phys 79(1):12
42. Kang S, Sotiropoulos F (2011) Flow phenomena and mechanisms in a field-scale experimental meandering channel with a pool-riffle sequence: insights gained via numerical simulation. J Geophys Res 116:F0301
43. Ge L, Sotiropoulos F (2007) A numerical method for solving the 3D unsteady incompressible Navier–Stokes equations in curvilinear domains with complex immersed boundaries. J Comput Phys 225:1782
44. Khosronejad A, Sotiropoulos F (2017) On the genesis and evolution of barchan dunes: morphodynamics. J Fluid Mech 815:117
45. Germano M, Piomelli U, Moin P, Cabot WH (1991) A dynamic subgrid-scale eddy viscosity model. Phys Fluids A 3(7):1760
46. Gilmanov A, Sotiropoulos F (2005) A hybrid Cartesian/immersed boundary method for simulating flows with 3D, geometrically complex, moving bodies. J Comput Phys 207:457
47. Jiang GS, Shu CW (1996) Efficient implementation of weighted ENO schemes. J Comput Phys 126(1):202
48. Sussman M, Fatemi E, Smereka P, Osher S (1998) An improved level set method for incompressible two-phase flows. Comput Fluids 27(5–6):663
49. Kang S, Sotiropoulos F (2012) Numerical modeling of 3D turbulent free surface flow in natural waterways. Adv Water Resour 40:23
50. Kang S, Sotiropoulos F (2015) Large-eddy simulation of three-dimensional turbulent free surface flow past a complex stream restoration structure. J Hydraul Eng 141(10):04015022
51. van Rijn LC (1984) Sediment transport, part II: suspended load transport. J Hydraul Eng 110(10):1431
52. Khosronejad A, Kozarek JL, Palmsten ML, Sotiropoulos F (2015) Numerical simulation of large dunes in meandering streams and rivers with in-stream rock structures. Adv Water Resour 81:45. https://doi.org/10.1016/j.advwatres.2014.09.007
53. Khosronejad A, Kozarek JL, Sotiropoulos F (2014) Simulation-based approach for stream restoration structure design: model development and validation. J Hydraul Eng 140(9):04014042. https://doi.org/10.1061/(ASCE)HY.1943-7900.0000904
54. Zech Y, Soares-Frãzao S, Spinewine B, Le Grelle N (2008) Dam-break induced sediment movement: experimental approaches and numerical modelling. J Hydraul Res 46(2):176
55. Khosronejad A, Hansen AT, Kozarek JL, Guentzel K, Hondzo M, Guala M, Wilcock P, Finlay JC, Sotiropoulos F (2016) Large eddy simulation of turbulence and solute transport in a forested headwater stream. J Geophys Res Earth Surf 121(1):146
56. Fredsoe J (1974) On the development of dunes in erodible channels. J Fluid Mech 60:1
57. Henderson FM (1966) Open channel flow. MacMillan Series in Civil Engineering